

Calibration of colour gradient bias in shear measurement using CANDELS

X. Er¹*, H. Hoekstra², T. Schrabback³, V. F. Cardone¹, R. Scaramella¹, R. Maoli⁴, M. Vicinanza^{1,4,5}, L. Miller⁶, J. Rhodes^{7,8}

¹ I.N.A.F. - Osservatorio Astronomico di Roma, via Frascati 33, 00040 - Monte Porzio Catone, Roma, Italy

² Leiden Observatory, Leiden University, PO Box 9513, NL-230 RA, Leiden, the Netherlands

³ Argelander Institut fuer Astronomie, Auf dem Huegel 71, D-53121 Bonn, Germany

⁴ Dipartimento di Fisica, Universita di Roma "La Sapienza", Piazzale Aldo Moro, 00185 - Roma, Italy

⁵ Dipartimento di Fisica, Universita di Roma "Tor Vergata", via della Ricerca Scientifica 1, 00133 - Roma, Italy

⁶ Department of Physics, Oxford University, keble Road, Oxford OX1 3RH, UK

⁷ Jet Propulsor Laboratory, California institute of Technology, 4800 Oak Grove Drive, Pasadena, CA 91109, USA

⁸ California Institute of Technology, 1200 East California Blvd, Pasadena, CA 91125, USA

Accepted –; received –; in original from 11 October 2016

ABSTRACT

In weak gravitational lensing, the precision strongly depends on the shape measurement of the galaxy images. Observation using wide band filter can provide images with high signal-to-noise ratio, and can cover a large redshift range as well. However, the shape measurement requires analysis of the point spread function (PSF). In general, both the PSF and the galaxy are chromatic, i.e. the shapes vary with wavelength. Thus, measuring the shape of galaxies using integrated images over the filter will cause higher order systematic bias, which is called colour gradient bias. We perform an estimate of this bias using both simulated images and real data from CANDELS. We show that the estimation for colour gradient bias using two narrow bands can reach a high precision in the simulated noisy data. The estimation using noisy images has a large scatter, which may over-estimate the magnitude of the bias. In our sample of real galaxy images, we find correlations between the bias with the colour and the size of the galaxy. Moreover, we find that the higher order image distortions, such as flexion, will enlarge the colour gradient bias in shear, although it affects the estimation only when the images are in strong lensing regions.

Key words: cosmology, weak lensing, systematics

1 INTRODUCTION

Weak gravitational lensing has been identified as a powerful method in cosmology, such as mapping the large scale structures. The images of distant galaxy are distorted by the gravitational potential generated by the intervening matter. A statistical analysis of image distortion of background galaxies provides crucial information about the mass distribution and thus tight constraint to the cosmological models (e.g. Bartelmann & Schneider 2001; Hoekstra & Jain 2008).

The precision of measuring the shapes of the galaxy images is limited due to the atmospheric turbulence, i.e. Point Spread Function (PSF). Thus space telescopes can take the advantage of small space PSFs, e.g. the future weak lensing survey loaded on the Euclid satellite. The weak lensing survey by Euclid plans to provide a large sample of accurate measurements of both shape and photometric redshift for the galaxies. The filter of the Euclid image

survey has a very wide bandpass (550nm – 920nm), which covers a large range of redshift of galaxies and can also obtain galaxy images with high signal-to-noise ratio (SNR).

In shear measurements, the galaxy shape is corrected using the effective (integrated) PSF. However, the galaxies in general have different intrinsic shapes at different wavelengths, as well as the PSF, e.g. the size of PSF is slightly larger at longer wavelength. (Meyers & Burchat 2015) have also shown that the differential chromatic refraction can introduce systematics to the measurement of galaxy shapes. The chromatic PSF causes a bias in the measurement, which can be estimated and reduced to the required levels using a colour weighted PSF (Cypriano et al. 2010). While the correction described in Cypriano et al. (2010) assumes a uniform spectral energy distribution (SED) of the source galaxy. It becomes inaccurate when the SED, or colour of the source galaxy varies spatially. The effects introduce a higher order systematic bias in measuring the shape of galaxies, if one uses the integrated images and integrated PSF. The bias, which we called colour gradient (hereafter CG) bias, has dependence on several factors: such as the

* er.xinzhong@oa-roma.inaf.it

SED of the galaxy, the relative size of the galaxy to the PSF, as well as the bandwidth of the filter. The relative magnitude of the CG can be neglected for narrow band survey. However, the CG bias is expected to be relevant for Euclid, especially since the error budget of Euclid weak lensing project is small (e.g. Cropper et al. 2013; Massey et al. 2013).

In (Voigt et al. 2012; Sembolini et al. 2013), the simulated images with Euclid features are used to study the CG bias. A potential bias of level 10^{-3} is found for typical size galaxies even with a smooth SED, i.e. without strong emission or absorption lines. Moreover, it has been shown that using two high resolution narrow band images, one can calibrate the CG bias with high precision for a specific subset of galaxies, e.g. the galaxies without strong emission/absorption lines. In this work, we will demonstrate the result and the method in Sembolini et al. (2013), and apply the calibration method to the simulated noisy images. The method requires that the match of the bandwidth and the smooth spectrum of the source galaxy. For the first point, the bandwidth of weak lensing survey on Euclid can be cover by two filters on the Hubble Space Telescope (HST), i.e., F606W and F814W. In the image simulation with smooth spectra, the calibration can reproduce the CG bias with high precision.

We also apply the method to a real set of galaxy images from HST CANDELS data (Schrabback et al. in prep.). A preliminary CG bias is presented. It is expected from star formation studies that colour and colour gradient of the galaxy are correlated (Welikala et al. in prep.), thus it is not a surprise to see that the CG bias has a correlation with the colour of source galaxy. In Section 3, we follow the result in Sembolini et al. (2013)(ES13 in the rest of this paper). We use simulated images to study the CG bias. In Section 4 we apply the calibration method using two band images from CANDELS data, and give our discussion and conclusion in the end.

2 BASIC FORMULISM

We introduce the basic symbols and parameters that will be used in this paper. We use angular coordinate θ on the lens plane, and $\gamma = \gamma_1 + i\gamma_2$ is the complex lensing shear. We consider an image of a galaxy, and denote the photon brightness distribution of the image at each wavelength λ by $I(\theta, \lambda)$, which is related to the intensity $S(\theta, \lambda)$ by $I(\theta, \lambda) = \lambda S(\theta, \lambda)$. Due to the PSF $P(\theta, \lambda)$ and filter of the telescope $F(\lambda)$, the image of a galaxy observed with a filter of width $\Delta\lambda$ is given by

$$I^{obs}(\theta) = \int_{\Delta\lambda} I(\theta, \lambda) * P(\theta, \lambda) F(\lambda) d\lambda, \quad (1)$$

where $*$ denotes a convolution. In the weak lensing regime, the shear can be estimated from the ellipticity of the source galaxy, which is usually a measurement of second order brightness moments Q_{ij} (Bartelmann & Schneider 2001)

$$e_1 + ie_2 \approx \frac{Q_{11} - Q_{22} + 2iQ_{12}}{Q_{11} + Q_{22} + 2(Q_{11}Q_{22} - Q_{12}^2)^{1/2}}, \quad (2)$$

where the second order brightness moments are given by

$$Q_{ij} = \frac{1}{S_0} \int I^{obs}(\theta) \theta_i \theta_j W(\theta) d^2\theta \quad (i, j = 1, 2), \quad (3)$$

where $S_0 = \int d^2\theta I^{obs}(\theta)$ is the total observed brightness, and $W(\theta)$ is the weight function. The moment-based methods, such as KSB (Kaiser et al. 1995) or DEIMOS (Melchior et al. 2011) will be biased due to the weight function, which causes dependence of the CG bias to the properties of weight function. In this paper, we will

limit the method to the brightness moments, and use the circular Gaussian weighting function with the size of half light radius.

The CG bias is estimated from following steps (see ES13 for more details): we first generate the image in each wavelength from the galaxy model. Then we shear the images, and apply the convolution with PSF before integrating over the wavelength. Since both the galaxy and the PSF are chromatic, the integrated image contains CG bias. We also need the uniform SED image, which contains non-colour gradient (NCG), that is the ideal image for shear measurement. In order to isolate the CG bias, the simulated CG image and the NCG image need to provide identical shear measurement, in case of achromatic PSF or without lensing. Therefore the NCG images can be generated by

$$I^{NCG}(k, \lambda_{ref}) = \frac{F(\lambda_{ref}) I^{obs}(k)}{P_{eff}}, \quad (4)$$

where $I^{obs}(k)$ is the galaxy image (Eq.1) in Fourier space. The deconvolution is performed with the effective PSF

$$P_{eff}(\theta) = \int d\lambda P(\theta, \lambda) F(\lambda), \quad (5)$$

which is the PSF integrated over the filer band. The NCG images are the uniform image over the wavelength. One can see Fig.1 for the steps of generating the CG and NCG images. We need to emphasize here that the images we generated to estimate the CG bias are independent of the measurement method. As we will shown in the appendix, in the moment method, if we convolve the two images with the same PSF, the ratio of the ellipticity from two images does not change. Comparing the ellipticity (shear) measured from the two images we will have the multiplicative CG bias (Heymans et al. 2006)

$$m = \frac{e_i^{CG}}{e_i^{NCG}} - 1, \quad (6)$$

where e_i refers to the measurement of the first or second component of the ellipticity. In principle, the two components e_1 or e_2 will give the same estimation of the CG bias. In case of the existence of intrinsic shape noise, or one of the shear components is extremely small, the CG bias may have a different response, which can be avoided by rotating the galaxy images. In this work, we will use one ellipticity component $e_1^{CG}/e_1^{NCG} - 1$ as our estimate if not specified. The additive bias can be detected by correlating the estimated shear and will not be considered here.

3 COLOUR GRADIENT BIAS IN SIMULATED DATA

The CG bias is a higher order systematic bias, the numerical noise in simulated images may cause extra error in our analysis. Thus, we first adopt two independent codes to generate the simulated images: C/C++ and python-based GalSim package (Rowe et al. 2015). In our C code, we directly calculate the brightness density at the centre of each pixel, and sample the image using the approximate brightness in each pixel (brightness at the centre multiply the area of pixel). In GalSim the image can be directly generated from subroutines in the package, which sample the image by FFT rendering. The circular images are used for the source galaxy. We check the initial mock image, and the ones after convolution and deconvolution. No significant ellipticity are found in neither C or GalSim. Since the deconvolution is particularly difficult in the numerical calculation, we also perform that for the elliptical images. A small

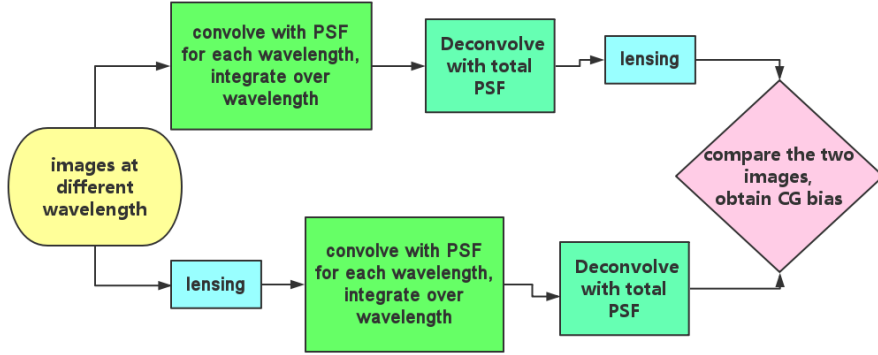


Figure 1. The steps of how we simulated CG (bottom flow) and NCG (top flow) images to estimate the shear CG bias.

relative error $\sim 10^{-6}$ appear in ellipticity using both C and GalSim, which is two orders of magnitude smaller than the possible CG bias.

We apply the same galaxy model as in ES13. It will allow us to further check the numerical error, since in ES13 the images are simulated by different code. The simulated galaxy images are consist of two components: bulge and disk, both are modeled by a Sersic profile with index n

$$I_{\text{Sersic}}(\theta) = I_0 e^{-\kappa \theta^{1/n}}, \quad (7)$$

where I_0 is the central intensity, and $\kappa = 1.9992 n - 0.3271$. For the SED of the bulge and the disk we use the galaxy templates from Coleman et al. (1980). The SED of the bulge is modelled by an elliptical galaxy, and SED of irregular galaxy for the disk. We choose an extremely blue SED for disk to generate large colour gradient in the galaxy images. For each wavelength, we construct the galaxy image $I(\theta, \lambda)$ by adding up the profiles of bulge and disk normalised by fixing the ratio $S_{\text{bulge}}/S_{\text{disk}}$ at $\lambda = 550\text{nm}$. The integrated profile is applied to the Euclid filter in a wavelength range $[550 : 920]\text{nm}$ with a step of 1nm. The images are constructed in an isolated stamp with size 256×256 pixels, and resolution 0.05 arcsec/pixel (Table 2).

We use different reference PSF models. The first one is a Gaussian profile, with wavelength dependent width:

$$\sigma_{\text{psf}}(\lambda) = w_{0,800} \left(\frac{\lambda}{800\text{nm}} \right), \quad (8)$$

where $w_{0,800}$ is the width of the PSF at 800nm. In this section we use $w_{0,800} = 0.102$ arcsec, which is the same as in ES13. The other reference model is an Airy function, which is close to the Design profile (Laureijs et al. 2011)

$$P(\theta) = \frac{I_0}{(1-\epsilon^2)^2} \left(\frac{2J_1(x)}{x} - \frac{2\epsilon J_1(\epsilon x)}{x} \right)^2, \quad (9)$$

where I_0 is the maximum intensity at the center, ϵ is the aperture obscuration ratio, and $J_1(x)$ is the first kind of Bessel function of order one. x is defined as $x = \pi\theta/l$, where $l = \lambda/D$ is wavelength over diameter ($\epsilon = 1/3$, $D = 1.2$ for Euclid). In Fig. 2, we compare the Airy model with other PSF models.

We measure the CG bias as a function of weight function size (Fig.3). The solid lines are the results from ES13, and the dashed (dotted) lines are the results using C (GalSim) code. The blue and

PSF	Description
Gaussian	Gaussian PSF described by Eq. 8 with $w_{0,800} = 0.102$
GaussianT	Gaussian core described by Eq. 8 with $w_{0,800} = 0.054$ plus top-hat with 20 percent of the total flux the cut-off size $\propto \lambda^{0.74}$ (ES13)
Airy	Airy model with obscuration 1/3 (Eq.9)

Table 1. The PSF models shown in Fig. 2. The Gaussian model, which is the same PSF model in ES13 is used for the simulated images. The GaussianT model is a Gaussian core plus a top hat function (ES13), which is shown as a comparison with Airy model. The Airy model is used for the bias calibration and HST data analysis in the following section.

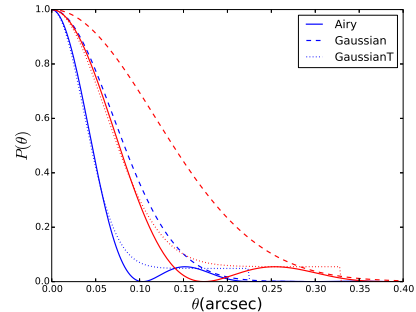


Figure 2. Comparison of the PSF models at 550nm (blue) and 920nm (red): the solid, dashed and dotted lines are the Airy, Gaussian and GaussianT PSF models respectively (Table 1).

green lines are the CG bias of small size galaxy (S-galaxy), while the red and purple lines are that of big size galaxy (B-galaxy). One can see that the CG bias from all three different simulated galaxies are consistent, i.e. the numerical error does not introduce significant bias in this study. Thus, in the following of this section, we will only use the GalSim to generate the mock galaxies. The CG bias decreases with the increasing weight size. As the optimal choice to maximize the signal-to-noise ratio is to match the weight function

Name	SED	axis(arcsec)	flux ratio (550nm)	Sersic index n
B-galaxy	E/Irr	0.17/1.2	1:3	1.5/1.0
S-galaxy	E/Irr	0.09/0.6	1:3	1.5/1.0

Table 2. Parameters of simulated galaxies: when two values are quoted in a column, the first refers to the bulge, the second to the disc.

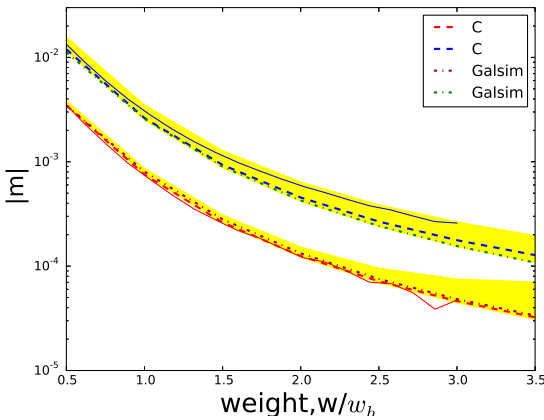


Figure 3. The CG bias in shear versus weight function. The solid lines are the results from paper ES13. The dashed (dash-dotted) lines are the results of this work using images simulated from C (GalSim) code. The blue (red) lines are the result for small (big) size simulated galaxies. The yellow shadow is the variation introduced by higher order image distortions. w_h is half light radius of the galaxy image.

to the size of the source galaxy, we will use the half light radius for the weight function in the following of this paper. For the two mock galaxies, the CG bias with such a weight function is 0.8×10^{-3} , 2×10^{-3} for B- and S-galaxy respectively. The smaller size galaxies have a larger CG bias, which suggests that the calibration of the CG bias need to take into account of the size as well as the real colour gradient of the galaxy.

In weak lensing, the main image distortion can be described by shear. The higher order effects, such as flexion (e.g. Goldberg & Natarajan 2002; Bacon et al. 2006) can also introduce image distortions. In our analysis, we only apply the shear effect in the lensing process, while the higher order image distortions also suffer from CG bias as well. In additional tests, we perform the complete lens ray-tracing instead of solely shearing the images. We adopt an Singular Isothermal Sphere halo model as the lens model, and vary the configuration within some reasonable range, such as the Einstein radius, and the separation between the lens and the source image (the corresponding shear value varies between about [0.02, 0.1]). We find that the variation of lensing magnitude can cause different CG bias (yellow shadow in Fig.3), and in most time the flexion effect will increase the CG bias. Such effects do not appear if we solely shear the images. However in general case, the cosmic shear has a value about a few percents. We can see that from the bottom boundary of the yellow shadow, the bias are almost the same as that only considering the shear effect. Only in case of the galaxy cluster lensing, galaxy-galaxy lensing, especially in the strong lensing region, when the shear and flexion become significant, one needs to take into account of such kind of effect.

3.1 Calibration of CG bias using simulated HST images

We outline the method that calibrate the CG bias using two bands images, while the details can be found in ES13. The main assumption of the validation for the method is that the galaxy can be decomposed into simple bulge and disk. For each of the narrower filter the deconvolved image can be approximated by:

$$I_i(\theta) = \int_{\Delta \lambda_i} T_i(\lambda) I^0(\theta, \lambda) d\lambda, \quad (10)$$

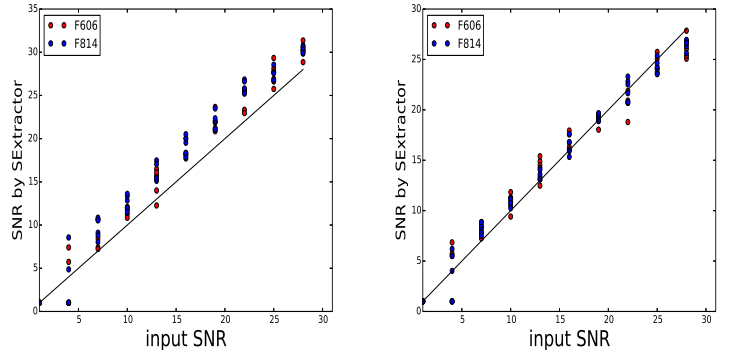


Figure 4. SNR estimated by SExtractor vs input SNR. Left is for the B-galaxy; Right is for the S-galaxy.

where $i = 1, 2$ stand for the two bands. We assume that for each pixel the image can be interpolated linearly:

$$I^0(\theta, \lambda) = a(\theta)\lambda + b(\theta). \quad (11)$$

The coefficients (a, b) can be solved from a linear system of equations:

$$T_{ai}\lambda a(\theta) + T_{bi}b(\theta) = I_i(\theta), \quad i = 1, 2, \quad (12)$$

where $T_{a,b,i}$ is the integrated transmission function at two filters. We will use the reconstructed image of each wavelength $I^0(\theta, \lambda)$ to estimate the CG bias as in the previous section.

The same two galaxy models from previous section are used in the simulation, and we simulate the images in two HST filters: F606W, F814W, which cover the filter of Euclid image survey. The spectra of the galaxy are shifted according to their redshift, but the evolution of the galaxy or the cosmology are not adopted in the simulation. The spatial resolution is 0.05 arcsec/pixel. The PSF is modeled by the Airy function with diameter $D = 2.5$ and obscuration 0.33, which is the configuration of HST. As shown in ES13, one needs to correct the PSF effect in the observed images, or the CG bias will be underestimated. We perform deconvolution for images before the bias estimation. It is a straightforward mathematical step for the simulated noise-free image. For the noisy image, the deconvolution will be difficult and causes serious numerical problems.

In order to see the effect of noise in the galaxy image, we add Gaussian noise into the simulated HST images. An ideal level (SNR=50) and a moderate level (SNR=15) are used to see the effect of the CG bias. The RMS of the Gaussian image noise is determined by the total flux (F_{tot}) within a certain radius $1.5 r_h$

$$\sigma = \frac{F_{tot}}{\text{SNR} \sqrt{N_{tot}}}, \quad (13)$$

where N_{tot} is the total pixel number within $1.5 r_h$. In Fig.4, we compare the input SNR with that estimated by SExtractor (Bertin & Arnouts 1996). We can see that the estimations are slightly higher than the input values, but for the case of $\text{SNR} = 15$, the estimations are within a reasonable value for real weak lensing survey.

Direct deconvolution of a noisy image will end with a strange galaxy image and large numerical noise, thus we apply Galfit (Peng et al. 2010) to fit the noisy image, and use the fitted image as our noise reduced observed image, i.e. the residual noise is not taken into account for CG analysis. For the necessary fitting profile and number of components, we use two Sersic components as

	S-606W	S-814W	B-606W	B-814W
n_1	0.5-2.5	0.5-2.5	0.5-2.5	0.5-2.5
n_2	0.5-2.5	0.5-2.5	0.5-2.5	0.5-2.5
R_{bulge}	1-10	1-10	3-30	3-30
R_{disk}	5-30	5-30	10-60	10-60
q	0.6-1	0.6-1	0.6-1	0.6-1

Table 3. Constraints for the fitting parameters in Galfit. The first two columns are for two images of the S-galaxy, the other two are the image of B-galaxy. n_1 is the Sersic index for bulge, and n_2 is the Sersic index for disk. The effect radius is given in unit of pixel (0.03 arcsec).

bulge and disk for both image bands. For each image, we apply further constraints to the galaxy parameters: Sersic index, effective radius, and axis ratio (Table 3). We compare fitting parameters with the input value for noisy images of different SNR. In general, the effective radius can be achieve at a small variations (within 20%), while the Sersic index usually has a large difference from the input values as well as scatter.

In order to provide a initial parameters for Galfit, we use the stacked image of two bands to estimate the center and some initial values of the galaxy parameters from SExtractor. The fitting images slightly depend on the initial values, and can effect the estimate for the CG bias estimation. The dependence will become significant with the decreasing of image SNR. In the following estimation for the CG bias, we will perform the image fitting using two kinds of initial parameters: in the first one we will leave all the fitting parameters free; while in the other one we will freeze the Sersic index as the simulated value, and leave the others free, since we will see that the Sersic index will only weakly affect the CG bias. As we will present, with sufficient large sample of noisy images, the estimation for the CG bias can converge despite of the initial parameters.

Applying the calibration method to the fitted images, we can obtain the estimation of the CG bias for the simulated images. In Figs.5 and 6, we show the shear CG bias with redshift. The black solid lines are the "true" CG bias directly using simulated image, i.e. from the true SED of galaxy rather than estimated from the two band images. The dashed lines are the estimation using two HST images without noise, and the colour lines use noisy images. For the red lines, we free all the parameters in image fitting, for blue lines we fix the Sersic index. For the orange lines we also free all the parameters, but we perform another convolution with the effective PSF (see appendix for more detail). In Fig.1 one can see that the convolution is canceled with the last deconvolution for the CG images. The reason for that is the deconvolution may cause some numerical errors, especially for the noisy images. Therefore, in the following result for noise images, we will perform the convolution to the NCG image instead of deconvolution to the CG one. (In reality we perform additional tests using images with $SNR=15$, and find the deconvolution does cause some numerical problems) Moreover, although we use the circular source image in the simulation, the fitted noisy images will become slightly elliptical. In order to get rid of the error due to the "intrinsic shape", we rotate the source image 6 times, and use the average value as our estimate for the galaxy ellipticity (Nakajima & Bernstein 2007). At each redshift, we use one noise free image and 40(200) noisy images for $SNR = 50(SNR = 15)$. In the bottom panel of each figure, we also show the residues with respect to the true CG bias, and the error bars, which are given by the standard deviation from e_{cg} and

$$e_{ncg}$$

$$\sigma_m = |m| \sqrt{\left(\frac{\sigma_{cg}}{\langle e_{cg} \rangle}\right)^2 + \left(\frac{\sigma_{ncg}}{\langle e_{ncg} \rangle}\right)^2}. \quad (14)$$

It is not surprising that our estimate can reproduce the properties of CG bias in ellipticity measurement using both ideal or noisy images, since the spectra of the source galaxies are relatively smooth. In the error panel, the grey shadow stands for the error budget of CG bias in Euclid cosmic shear analysis (± 0.00025 Cropper et al. 2013; Massey et al. 2013). The scatters in the estimation are proportional to the magnitude of the bias, i.e. we have large uncertainty for S-galaxy at low redshift. In preliminary tests using other measurement methods for PSF correction, such as the image fitting methods (e.g. Miller et al. 2007; Kitching et al. 2008; Miller et al. 2013), and KSB+ (e.g. Hoekstra et al. 1998; Heymans et al. 2006), the bias has similar dependence on the SED of the galaxies.

In the figures, we can see that at $z = 0.5$ and 0.9 , the estimate is significantly smaller than the true value for both galaxy models. This is due to the uneven SED of the source galaxy in the two HST filter. In Fig.7, we compare the SED of the galaxy in redshift $z = 0, 0.5$. One can see that at $z = 0.5$, besides the strong emission lines, the linear approximation will cause significant error in the estimation as well.

3.2 PSF variations

In the previous test, we used an ideal circular symmetric Airy PSF model. It may however cause inaccuracy in our estimation of the CG bias. Thus, we perform additional tests due to the variations of the PSF. The noise free images are used in order to isolate the effects of the PSF. The different PSF models are applied only in the step of deconvolution for the identical simulated images, since this is the step we need the observed PSF in analysis of real data.

We generate three pairs of PSFs by increasing the wavelength by 10% in the Airy model, which increases the size of PSF slightly. The effect on the CG bias is shown in Fig.8. From solid, dashed to dotted lines, we increased the PSF size of the F606 bands; while from red, green to blue lines, we increase the PSF size of the F814 bands. Although the effect due to the two PSF variations depends on the SED of the source galaxy, one can see that increasing the size of the PSF in different bands will cause either an increase or decrease in the CG bias calibration. Once again, we can see that the small galaxies are more sensitive to the variation of PSF.

Moreover, we generate 3 different PSF models using TinyTim (Krist et al. 2011): the first one is a normal PSF without defocus, the second one is a bit larger but still realistic PSF, which is generated by changing the parameter defocus offset of secondary mirror to the primary, the third one is simply transposing of the first one. In Fig.9, we do not find significant effects with slight variations on the PSF. This may be because we used the circular symmetric, noise free images in the tests. For real galaxy noisy images, the PSF may cause slightly stronger effects. In additional tests, we calculate circular averages of the three PSF models, and find slightly different CG bias when using the second model PSF, since it has slightly larger size. Thus, the limited accuracy of the PSF model is not an important source of error in our study.

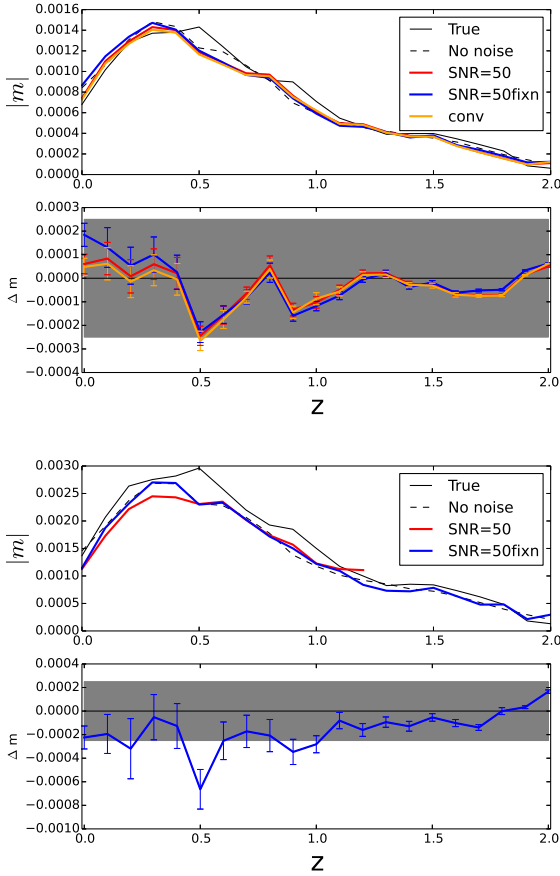


Figure 5. The CG bias in shear measurement as a function of redshift using simulated images. The black solid lines are the true CG bias; the dashed lines are the estimation using two band HST images without noise; the colour lines are the estimation using noisy images of input $SNR = 50$, the value are the average over 40 realizations each redshift. In the bottom, Δm is the residual with respect to the true CG bias, and the error bars show the standard variations (Eq.14). Up(Down)-figure are the results for B-(S-)galaxy.

4 CANDELS DATA

4.1 Calibration sample

In this section, we use the real galaxy images to estimate the CG bias which will appear in the Euclid weak lensing survey. For the reference PSF, we use the Airy model (Eq. 9).

To investigate the impact of colour gradients using realistic galaxies populations, we employ HST/ACS data taken in the F606W and F814W filters in the three CANDELS fields (AEGIS, COSMOS, and UDS), which have a roughly homogeneous coverage in both bands (see Davis et al. 2007; Grogin et al. 2011; Koekemoer et al. 2011). We base our analysis on a tile-wise reduction of the ACS data, incorporating pointings which have at least four exposures to facilitate good cosmic ray removal, yielding combined exposure times of 1.3–2.3ks in F606W and 2.1–3.0ks in F814W. We employ the updated correction for charge-transfer inefficiency from Massey et al. (2014), MultiDrizzle (Koekemoer et al. 2003) for the cosmic ray removal and stacking, as well as careful shift refinement, optimised weighting, and masking for stars and image artefacts as detailed in Schrabback et al. (2010). Schrabback et al. (in prep.) describe the generation of weak

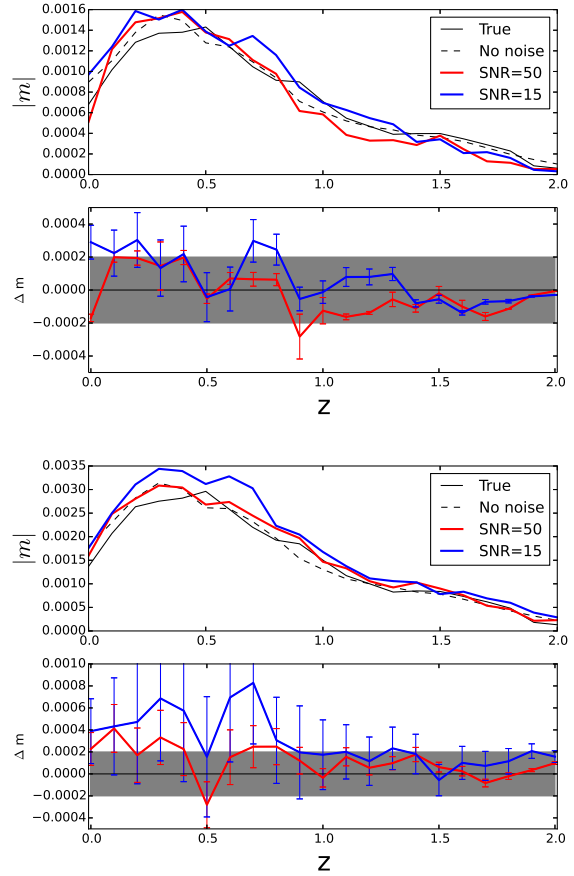


Figure 6. Same as Fig.5 but for images of $SNR=15$, and ??? realizations at each redshift.

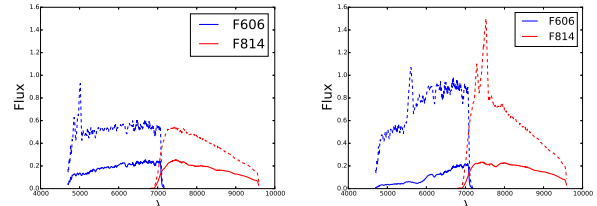


Figure 7. Spectral energy distributions used to create the disc and bulge components of our mock galaxies. They are normalized at $\lambda = 5500\text{\AA}$ by ratio $F_{\text{bulge}}/F_{\text{disk}} = 1/3$, and they are convolved with HST filter function in F606W and F814W. *left-* redshift 0; *right-* redshift 0.5.

lensing catalogues for these images. We base our analysis on the galaxies passing their source selection and apply additional magnitude cuts as detailed below. To investigate the dependence of the colour gradient influence on galaxy colour and redshift, we match this galaxy catalogue to the photometric redshift catalogue from Skelton et al. (2014). We list the total non-masked areas in which these catalogues overlap in Table 4.

We match the galaxy from V(F606W) and I(F814W) bands by selecting that the difference of galaxy coordinates in two bands is smaller than 1 pixel (0.05 arcsec). Moreover, in order to resemble the Euclid image survey, we apply selection based on the magnitude of two bands. In the first selection, the galaxy must be brighter than magnitude 25 in V-band and 24.5 in I-band. In the second se-

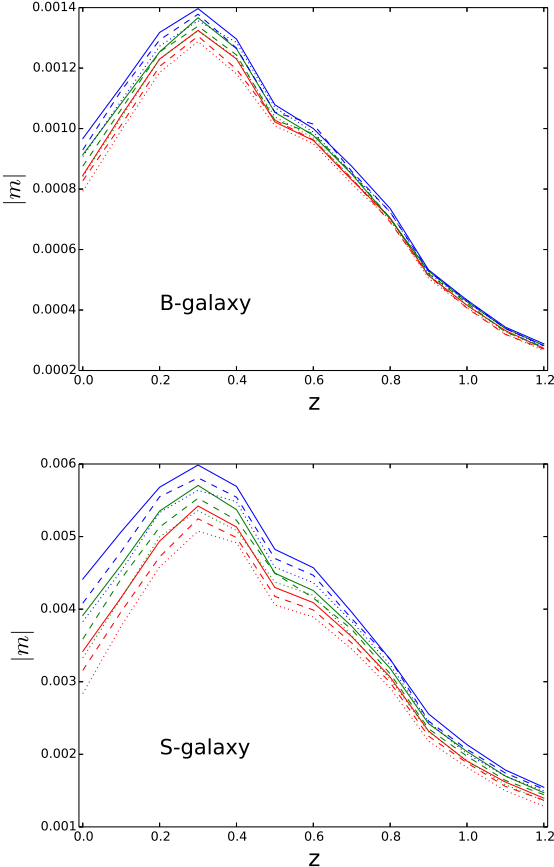


Figure 8. The PSF in the deconvolution are varied to see the effect on the CG bias. From red, green to blue lines, we increase the size of PSF for the F814W; from the solid, dashed to dotted lines we increase the size of PSF for the F606W.

lection (VIS, N2 sample), we apply the linear interpolation from V and I band using the effective wavelength to approximate the Euclid VIS magnitude, and select the galaxy brighter than 24.5 in VIS. In the last one (N3 sample), we enlarge the sample by using lower threshold in two bands: 25.5 in V and 25.0 in I band. The amount of galaxies is listed in Table 4. The galaxy VIS magnitudes will be determined by several factors, such as exposure time and filter transmission, etc. Thus, the actual number of galaxies can be different from what we have shown in this work. The approximation that we use rely on the flatness of the source spectrum. In the VIS sample, the number of galaxies is similar to that in the first selection in all three fields, which suggest that the spectra of our galaxies are relatively smooth. In the N3 sample the galaxy number is much higher. The total galaxy number and number density ($\sim 12/\text{arcmin}^2$) is lower than that in ES13 for several reasons: the galaxies are selected which the 3D-HST photometric redshift are available, and those suitable for weak lensing analysis, e.g. the very big or bright galaxies are not include. Moreover, in ES13 the galaxies are selected by the magnitude of F814W. However we select galaxies by the estimated VIS magnitude and well match in F606W and F814W.

There is no significant difference found in the distribution of galaxy parameters, such as effective radius, axis ratio, photometric redshift and colour (we use $m_{F606} - m_{F814}$ as colour in this work, and will write as m_{V-I} for short later). The SNR of most images

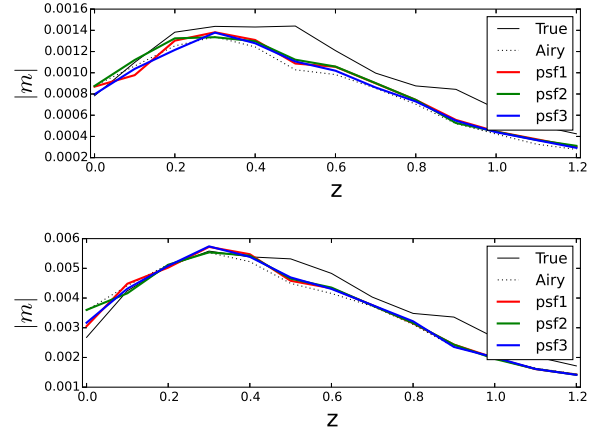


Figure 9. Same as Fig. 8 but using three different TinyTim PSF model. Top (Bottom) is for the B-galaxy (S-galaxy).

Field	Area (arcmin^2)	N_1	N_2	N_3
AEGIS	180	2094	2112	3460
COSMOS	139	1593	1656	2449
UDS	146	1455	1497	2341
Total	465	5142	5265	8250

Table 4. Size of the HST CANDELS data sample in F606W and F814W bands. The number of galaxies are shown in three selection methods to match the Euclid survey, $N_1: m_V < 25$ and $m_I < 24.5$, $N_2: m_{V\text{IS}} < 24.5$, $N_3: m_V < 25.5$ and $m_I < 25$.

in VIS sample are larger than 15, while in the N3 sample there are significant number of galaxies with $\text{SNR} \sim 10$. From the result of our simulations (Fig. ??), the images in the VIS sample can give relatively stable estimate for CG bias, while the low SNR images may suffer from large uncertainty of bias estimation. Thus we only show the result in the VIS sample.

We also compare the galaxies from 3 catalogues (AEGIS, COSMOS, UDS). In the distribution of galaxy parameters (Fig. 10), we find no significant difference in half light radius (r_h), galaxy axis ratio or redshift distribution. However, in the colour distribution, there are more blue galaxies (small m_{V-I}) in AEGIS, which is more significant in N3 sample. We will see later that the colour of galaxy is also related to the CG bias in shape measurement.

4.2 CG bias from CANDELS

We estimate the CG bias following the same procedure for the simulated galaxy:

- fit the galaxy using one Sersic component for both band images. Some constraints such as Sersic index ($0.5 < n < 3.5$), effective radius ($1 < r_e < 50$ pixel) and axis ratio ($0.6 < q < 1.0$) are adopted in Galfit.
- interpolate the SED on each pixel of the galaxy image, and generate the galaxy at each wavelength (Eq. 10 - 12), and then integrate over the wavelength to simulate the CG and NCG galaxy image.
- measure the shape of two images and calculate the bias m . We also apply 6 different orientation of the images in order to reduce the intrinsic shape noise (Nakajima & Bernstein 2007).

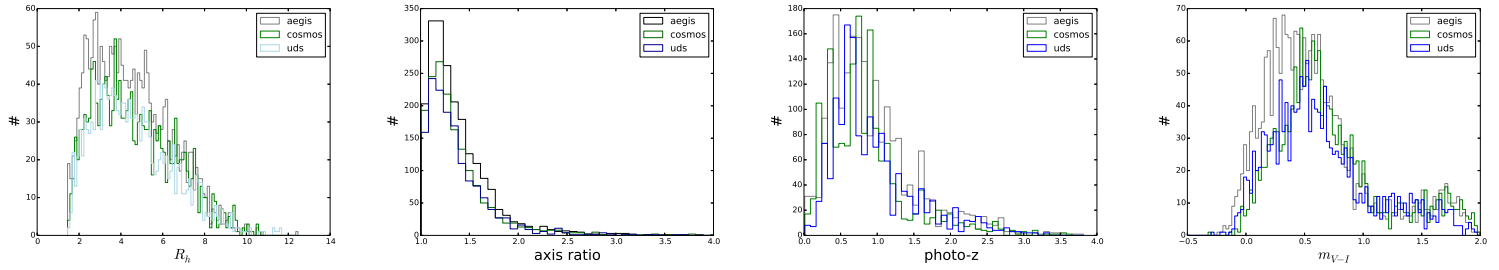


Figure 10. The histogram for basic galaxy properties in our sample. The lines with different colours represent galaxies from different catalogues (AEGIS, COSMOS, UDS). From left to right: half light radius, axis ratio, photometric redshift, and colour (m_{V-I}).

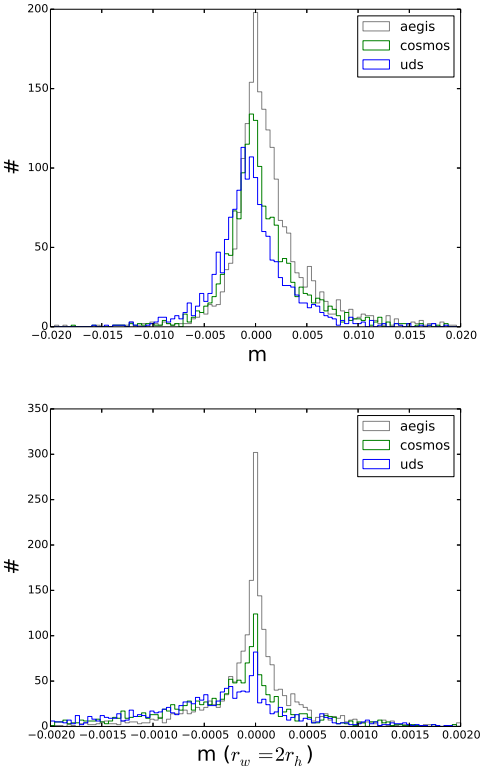


Figure 11. CG bias histogram from CANDELS: different colours show the result from three catalogues. In the bottom panel we show the CG bias using different weight function ($r_w = 2r_h$).

In Fig.11, we show the histogram of the CG bias. The CG bias in most of the galaxies is smaller than 0.01. We did not perform averaging as we did for the simulated noisy images, which can further reduce the scatter of the bias. Thus the actual bias, especially the scatter in the sample, is smaller. In the bottom panel, we estimate the CG bias using a larger weight function ($2r_h$). As one expected, the bias decreases by about one order of magnitude.

Three PSF models from TinyTim, which are the same as in the previous section, are used in the deconvolution (Fig.12). Slight difference are found among them. The bias using PSF2 are slightly higher than that using the other two models, since the size of PSF2 is larger. But no significant dependence on the PSF model is found with the relation of CG bias or galaxy parameters. The following results are shown using the first PSF model from TinyTim. Similar results are actually found when using the other two PSF models.

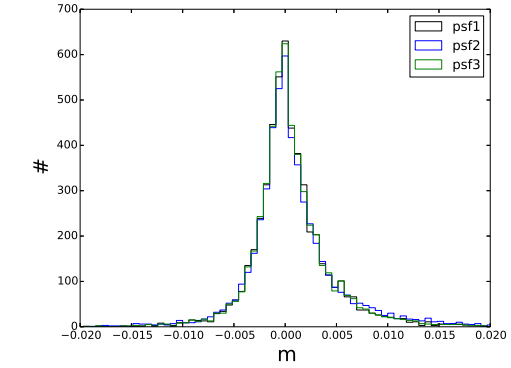


Figure 12. CG bias histogram of CANDELS using three different PSF models from TinyTim.

In order to find a quick estimation for the CG bias, we try to find the relation between CG bias with galaxy parameters. In Fig.13, one can see the CG bias with the fitting parameters from two band images. As we mentioned, the Sersic index is a difficult parameter to fit. Fortunately, in our simulation using noisy images, we find that the large scatter of the fitted Sersic index does not strongly affect the estimate of the CG bias. Similar in our sample of galaxies, we do not find any obvious relation between CG bias and Sersic index. On the other side, similar as in the simulation, the effective radius can be fitted more precisely, and we see that there is an approximately linear relation between the effective radius and CG bias. Moreover, one expect that when $r_{e606} = r_{e814}$, the CG bias in principle will be vanish, since the identical images from two bands will not have a colour gradient. In Fig.13, the blue lines are the binned average CG bias. In the bottom panel, one can see that the average bias meets zero at $r_{e814}/r_{e606} = 1$ as expected. However, in the Euclid VIS image survey, we will have only one band images, we thus need other methods for the bias estimation.

In Fig.11, the galaxies in AEGIS field have more positive CG bias than the galaxies in the other two. The colour distribution in AEGIS is different from the other two as well, which suggests the correlation bewteen the CG bias and the colour of the galaxy. In Fig.14, we show the relation between the CG bias and the colour of the galaxies. The bias is inversely proportional to the colour of the galaxies. The galaxy sample is split into two groups according to their colour: the red galaxies ($m_{V-I} > 0.5$) and the blue ones ($m_{V-I} < 0.5$). They are shown in the bottom panel of Fig.14 as a function of redshift. Most of the red galaxies are located at moderate redshifts, mainly between redshift [0.5, 1.0], while the blue galaxies are either at the lower redshift ($z < 0.5$) or higher

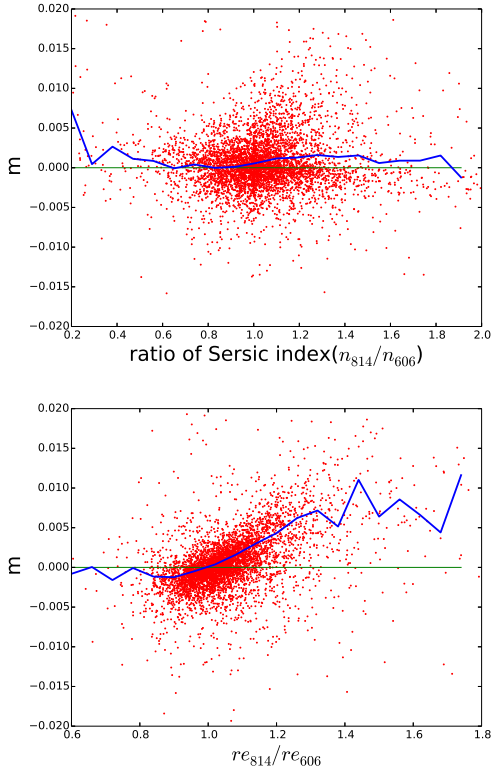


Figure 13. CG bias as a function of galaxy properties: ratio of Sersic index between two band (top) and effective radius between two bands (bottom). The blue lines are the average CG bias over the parameter bins.

redshift ($z > 1.0$). The CG bias in red galaxies are obviously more negative than that of the blue ones.

In Fig.15, we show the bias as a function of our mock VIS magnitude (m_{VIS}). There is no obvious dependence on m_{VIS} . However, the actual m_{VIS} is different from our linear approximation. Moreover, we stack the images from two bands as our mock VIS band images. Fig.16 shows the CG bias with the effective radius fitted from the VIS images. The blue line is the bin average. As one expects, the small size galaxies have larger bias than the big ones. A quick fitting formula for the bias can be found based on the effective radius and colour

$$\tilde{m} = a m_{V-I} \exp\left(\frac{-r_e^2}{625}\right) + \frac{b}{r_e^2}, \quad (15)$$

where r_e is the effective radius of wide band image, and $a = -1.5 \times 10^{-3}$, $b = 0.04$. The yellow shadow in Fig.16 presents the coverage of Eq.15 for $m_{V-I} \in [-0.2, 2]$ and $r_e \in [2, 50]$, which covers most of the bias.

The VIS images alone can provide an estimation for CG bias, e.g. the bias of small galaxy approximatively proportional to $1/r_e^2$. The VIS magnitude cannot provide any constraints solely. However, the multi-band magnitudes, i.e. colour, are correlated with the bias (Fig.14). Thus, one wide band image with multi-band photometries are necessary in order to reduce the CG bias. Moreover, the multi-band information is required for the photometric redshift study. One can obtain that for free to calibrate the CG bias. Although the dependence on the multi-band is different between photometric redshift and CG bias, the experience from photometric redshift can be used for CG bias, such as some machine learning algorithms. In the other two selection samples (N1, N2), we have

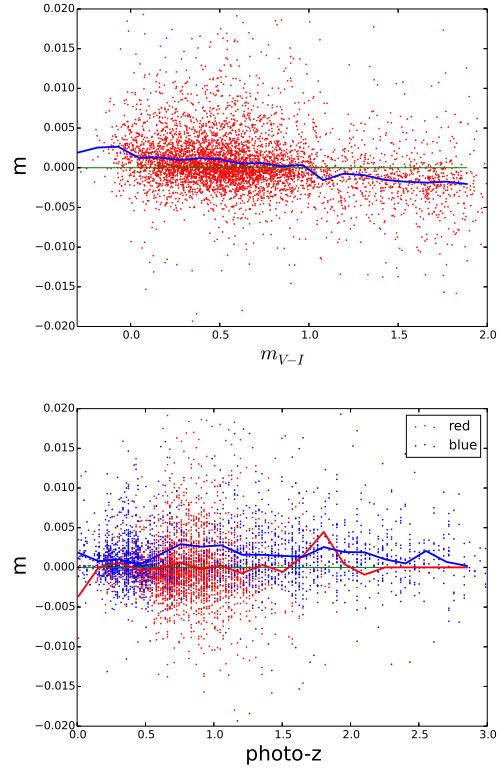


Figure 14. CG bias as a function of galaxy properties, top: color (m_{V-I}), bottom: photo-z. In the bottom panel, the red and blue points are the bias for red ($m_{V-I} > 0.5$) and blue ($m_{V-I} < 0.5$) galaxies respectively. The lines are the average CG bias in the redshift bins.

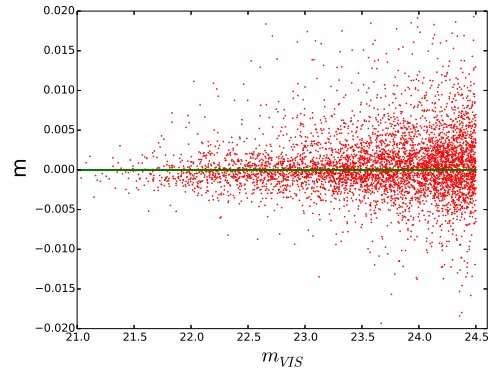


Figure 15. CG bias as a function of mock VIS magnitude.

found similar behaviours of the CG bias with the colour and effective radius of the galaxies.

We calculate the average bias over the redshift bins for both red and blue galaxies (Table 5). The red galaxies are mainly located between redshift (0.4, 1.2), while the blue galaxies are less in redshift (0.8, 1.2). The bias from red galaxies are significantly smaller than that of blue galaxies, as one expected, the colour gradient in the elliptical galaxies are smaller. The dispersions of the bias in each bin are slightly large, since the size of the galaxy can also affect the bias. Therefore, in order to calibrate the bias with high precision, one need more galaxy samples, especially the blue ones.

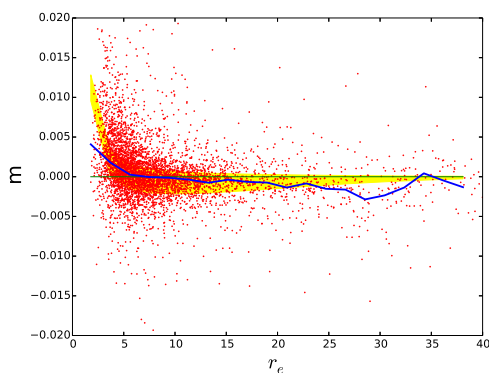


Figure 16. CG bias with effective radius from the stacked images. The unit of radius is a pixel ($= 0.05 \text{ arcsec}$). The blue line is the average over the radii bin, and the yellow shadow is the coverage by Eq.15.

photo-z	Number	\bar{m}	σ_m
0 – 0.4	187	-2.0×10^{-4}	0.0067
0.4 – 0.8	1415	-1.3×10^{-5}	0.0036
0.8 – 1.2	1116	1.3×10^{-4}	0.0047
> 1.2	245	-1.5×10^{-4}	0.0063
0 – 0.4	667	1.0×10^{-3}	0.0035
0.4 – 0.8	513	8.7×10^{-4}	0.0035
0.8 – 1.2	187	2.9×10^{-3}	0.0071
> 1.2	935	1.5×10^{-3}	0.0047

Table 5. The number, average CG bias and dispersion in redshift bins for blue (bottom half) and red (top half) galaxies.

In particular, the number density of blue galaxy between redshift [0.8, 1.2] is low.

5 SUMMARY AND DISCUSSION

In the image survey for weak gravitational lensing, the wide band filter can provide high signal-to-noise images and large coverage of redshift range. There is however a shape bias due to the chromatic shape of galaxy and the PSF, which is named as colour gradient bias. For very wide band surveys, such as Euclid, this effect can cause a non-negligible bias. In this work, we exam such a kind of bias in measuring the shape of a galaxy using both simulated images and real data taken from the HST ACS CANDELS survey. In the simulated galaxy images, we confirm the bias behaviour from previous results (ES13). We further apply the calibration method to the noisy images in the simulations, and find that with reasonable signal-to-noise ratio (SNR= 15) and numbers of galaxies (50 images for one type of galaxy in one redshift bin), we can estimate the CG bias to a high precision. However, the underestimate cannot be avoided due to strong emission lines, or the uneven SED of source galaxies. Moreover, the SNR of the simulated images in two bands are assumed to be the same. In reality, the signal-to-noise in different bands are correlated to the colour of the galaxies. We also apply the calibration method to the galaxy images taken by HST in two filters (F606W, F814W). In the estimation using CANDELS data, we find that most of the CG bias (m) is smaller than 0.01. The bias can be either over- or under-estimated. As we find from simulated images, the estimation using noisy image has a large scatter, thus

the CG bias in reality may be smaller than that shown here. On the other hand, the uneven spectrum of the galaxy causes a large CG bias.

In our sample of galaxies, the CG bias shows a correlation with the colour of galaxies. Since the bias depends on the size of the galaxies as well, we propose a fitting formula for the bias from the colour and effective radius of the galaxy. The fitting is limited to the galaxies in our sample, which need further investigation for different type of galaxies. The photometry from several bands, which will be used to estimate the redshift, can be also use for the CG bias analysis. Although the redshift dependence is not significant in our sample of galaxies, this may not be the case for a larger survey. In order to fully calibrate the bias for different redshift, a larger sample is essentially necessary. Moreover, in the weak lensing study, the colour of galaxies can be also used for the intrinsic alignment analysis. There is a potential correlation between the CG bias and the intrinsic alignment noise.

In our analysis of the CANDELS data, the environmental effect is not taken into account. Close galaxy pairs or nearby bright star(s) will also cause brightness/colour gradient, which will affect our estimate for CG bias. The significance of the environmental effect is still unknown, and may need further study. Moreover, in the calibration we linearly interpolate the SED on pixels from two bands. Some advanced method to estimate the SED (e.g. Joseph et al. 2016) may help to improve the calibration of the bias.

In this work, we use the brightness moments to estimate the ellipticity of the galaxy. The PSF correction is not taken into account. The bias thus will appear in any method of measurement. However, the bias using the measurement method for real data will be different, since every method has its own property and weight function. The CG bias will have method-dependent properties as well, although they will in principle have same dependence on the colour gradient of the galaxy images. As the first step of the CG bias analysis, we did not adopt any specific method in order to obtain general properties of the CG bias. Before the real analysis of Euclid data, one needs to study the bias with specific methods and simulated images with real properties in the Euclid weak lensing survey.

Moreover, as we point out that higher order image distortions, such as flexion may increase the CG bias. It can be seen from our analysis using both simulated and CANDELS data. Although the higher order effect can be neglected most times, it can still significantly increase the CG bias when the source images are located close to the strong lensing region. Therefore, such a kind of effect may cause significant bias in the strong lensing analysis using wide band images. In galaxy-galaxy lensing and cluster lensing, one needs to be careful about such higher order effects as well.

ACKNOWLEDGMENTS

We would like to thank Bryan Billis for helping on TinyTim PSF models, Emiliano Merlin, Marco Castellano for helping on SExtractor and Galfit, Gary Bernstein, Adam Rogers, Junqiang Ge and also in general, the members of the Euclid Consortium for useful discussions. XE and VFC are funded by Italian Space Agency (ASI) through contract Euclid -IC (I/031/10/0) and acknowledge financial contribution from the agreement ASI/INAF/I/023/12/0. XE is also partly support by NSFC Grant No. 11473032. JR is supported by JPL, which is run by Caltech under a contract for NASA, and is supported by grant NASA ROSES 12-EUCLID12-0004. The fast Fourier transforms are supplied by the FFTW li-

brary (Frigo & Johnson 2005). We use CFITSIO (Pence 1999) for the FITS file.

APPENDIX A: RATIO OF MOMENT VS. PSF CONVOLUTION

In general, the PSF correction will cause extra bias in the shear estimation. In order to isolate the CG bias, we measure the brightness moments without applying any PSF correction methods in this work, i.e. the CG bias will appear in any method. Moreover, the definition of our CG bias uses the ratio of ellipticity from images, thus the estimate for the CG bias will not be changed by the convolution of a small PSF. Let us denote the quantity with prime for those convolved with PSF, i.e.,

$$I'(\theta) = \int d^2\psi I(\theta)P(\theta - \psi). \quad (\text{A1})$$

The weighted brightness moment can be written as

$$Q_{ij} = \int d^2\theta W(\theta) f_{ij}(\theta)I(\theta), \quad (\text{A2})$$

$$Q'_{ij} = \int d^2\theta W(\theta) f_{ij}(\theta) \int d^2\psi I(\psi)P(\theta - \psi), \quad (\text{A3})$$

where $f_{ij}(\theta)$ is the function to characterize the brightness moments, e.g. $f_{ij}(\theta) = \theta_i \theta_j$ for the second order moment. We can replace the variable ψ by $r = \theta - \psi$, and Taylor expand with respect to ψ . Then the moment becomes

$$\begin{aligned} Q'_{ij} &= \int d^2\theta W(\theta) f_{ij}(\theta) \int d^2r I(\theta - r)P(r) \\ &\approx \int d^2\theta W(\theta) f_{ij}(\theta) \int d^2r P(r) \left[I(\theta) - \frac{\partial I(\theta)}{\partial r} r \right], \\ &= Q_{ij} \int d^2r P(r) - \int d^2\theta W(\theta) f_{ij} \int d^2r P(r) \frac{\partial I}{\partial r} r. \end{aligned} \quad (\text{A4})$$

The integral of $P(r)$ in the first term independent of the image of the galaxy, and equals to unity for normalised PSF. In case of circular symmetric PSF or the asymmetry is small, the second term can be neglect. $Q'_{ij} \approx p Q_{ij}$, where p is only determined by the size of PSF. Thus, for small PSF we have the approximation

$$\frac{Q'^{cg'}_{ij}}{Q^{ncg'}_{ij}} \approx \frac{Q^{cg}_{ij}}{Q^{ncg}_{ij}}, \quad (\text{A5})$$

which means that the small circular PSF will not change the CG bias in our definition.

REFERENCES

- Bacon, D. J., Goldberg, D. M., Rowe, B. T. P., & Taylor, A. N. 2006, MNRAS, 365, 414
- Bartelmann, M. & Schneider, P. 2001, Phys. Rep., 340, 291
- Bertin, E. & Arnouts, S. 1996, A&AS, 117, 393
- Coleman, G. D., Wu, C.-C., & Weedman, D. W. 1980, ApJS, 43, 393
- Cropper, M., Hoekstra, H., Kitching, T., et al. 2013, MNRAS, 431, 3103
- Cypriano, E. S., Amara, A., Voigt, L. M., et al. 2010, MNRAS, 405, 494
- Davis, M., Guhathakurta, P., Konidaris, N. P., et al. 2007, ApJ, 660, L1
- Frigo, M. & Johnson, S. G. 2005, Proceedings of the IEEE, 93, 216, special issue on “Program Generation, Optimization, and Platform Adaptation”
- Goldberg, D. M. & Natarajan, P. 2002, ApJ, 564, 65
- Grogan, N. A., Kocevski, D. D., Faber, S. M., et al. 2011, ApJS, 197, 35
- Heymans, C., Van Waerbeke, L., Bacon, D., et al. 2006, MNRAS, 368, 1323
- Hoekstra, H., Franx, M., Kuijken, K., & Squires, G. 1998, ApJ, 504, 636
- Hoekstra, H. & Jain, B. 2008, Annual Review of Nuclear and Particle Science, 58, 99
- Joseph, R., Courbin, F., & Starck, J.-L. 2016, A&A, 589, A2
- Kaiser, N., Squires, G., & Broadhurst, T. 1995, ApJ, 449, 460
- Kitching, T. D., Miller, L., Heymans, C. E., van Waerbeke, L., & Heavens, A. F. 2008, MNRAS, 390, 149
- Koekemoer, A. M., Faber, S. M., Ferguson, H. C., et al. 2011, ApJS, 197, 36
- Koekemoer, A. M., Fruchter, A. S., Hook, R. N., & Hack, W. 2003, in HST Calibration Workshop : Hubble after the Installation of the ACS and the NICMOS Cooling System, ed. S. Arribas, A. Koekemoer, & B. Whitmore, 337
- Krist, J. E., Hook, R. N., & Stoehr, F. 2011, in Society of Photo-Optical Instrumentation Engineers (SPIE) Conference Series, Vol. 8127, Society of Photo-Optical Instrumentation Engineers (SPIE) Conference Series, 0
- Laureijs, R., Amiaux, J., Arduini, S., et al. 2011, ArXiv: 1110.3193
- Massey, R., Hoekstra, H., Kitching, T., et al. 2013, MNRAS, 429, 661
- Massey, R., Schrabback, T., Cordes, O., et al. 2014, MNRAS, 439, 887
- Melchior, P., Viola, M., Schäfer, B. M., & Bartelmann, M. 2011, MNRAS, 412, 1552
- Meyers, J. E. & Burchat, P. R. 2015, ApJ, 807, 182
- Miller, L., Heymans, C., Kitching, T. D., et al. 2013, MNRAS, 429, 2858
- Miller, L., Kitching, T. D., Heymans, C., Heavens, A. F., & van Waerbeke, L. 2007, MNRAS, 382, 315
- Nakajima, R. & Bernstein, G. 2007, AJ, 133, 1763
- Pence, W. 1999, in Astronomical Society of the Pacific Conference Series, Vol. 172, Astronomical Data Analysis Software and Systems VIII, ed. D. M. Mehringer, R. L. Plante, & D. A. Roberts, 487
- Peng, C. Y., Ho, L. C., Impey, C. D., & Rix, H.-W. 2010, AJ, 139, 2097
- Rowe, B. T. P., Jarvis, M., Mandelbaum, R., et al. 2015, Astronomy and Computing, 10, 121
- Schrabback, T., Hartlap, J., Joachimi, B., et al. 2010, A&A, 516, A63
- Semboloni, E., Hoekstra, H., Huang, Z., et al. 2013, MNRAS, 432, 2385
- Skelton, R. E., Whitaker, K. E., Momcheva, I. G., et al. 2014, ApJS, 214, 24
- Voigt, L. M., Bridle, S. L., Amara, A., et al. 2012, MNRAS, 421, 1385